Nano Research

ISSN 1998-0124 CN 11-5974/O4
https://doi.org/10.1007/s12274-019-2517-2

Research Article

Butterfly-wing hierarchical metallic glassy nanostructure for surface enhanced Raman scattering

Hongyu Jiang[1,2], Jing Li[3], Chengrong Cao[1], Xiaozhi Liu[1,2], Ming Liu[1,2], Yutian Shen[1,2], Yanhui Liu[1,4], Qinghua Zhang[1,4], Weihua Wang[1,2,4], Lin Gu[1,2,4] (✉), and Baoan Sun[1,2,4] (✉)

[1] *Institute of Physics, Chinese Academy of Sciences, Beijing 100190, China*
[2] *School of Physical Sciences, University of Chinese Academy of Sciences, Beijing 100049, China*
[3] *Key Laboratory of Photochemical Conversion and Optoelectronic Materials, Technical Institute of Physics and Chemistry, Chinese Academy of Sciences, Beijing 100190, China*
[4] *Songshan Lake Materials Laboratory, Dongguan 523808, China*

Received: 19 June 2019 / **Revised:** 13 September 2019 / **Accepted:** 13 September 2019

ABSTRACT

The surface-enhanced Raman spectroscopy (SERS) is a technique for the detection of analytes on the surface with an ultrahigh sensitivity down to the atomic-scale, yet the fabrication of SERS materials such as nanoparticles or arrays of coinage metals often involve multiple complex steps with the high cost and pollution, largely limiting the application of SERS. Here, we report a complex hierarchical metallic glassy (MG) nanostructure by simply replicating the surface microstructure of butterfly wings through vapor deposition technique. The MG nanostructure displays an excellent SERS effect and moreover, a superhydrophobicity and self-cleaning behavior. The SERS effect of the MG nanostructure is attributed to the intrinsic nanoscale structural heterogeneities on the MG surface, which provides a large number of hotspots for the localized electromagnetic field enhancement affirmed by the finite-difference time-domain (FDTD) simulation. Our works show that the MG could be a new potential SERS material with low cost and good durability, well extending the functional application of this kind of material.

KEYWORDS

metallic glassy, structural heterogeneities, surface enhanced Raman scattering, superhydrophobicity, butterfly wing

1 Introduction

Surface-enhanced Raman spectroscopy (SERS) could detect the trace amounts of chemical species on surfaces with ultrahigh sensitivity down to the single molecular level, and has been widely used in a variety of fields including polymer and material science, biosensing, catalysis, and electrochemistry [1–3]. The principle of SERS is to utilize the optical resonance properties of nanostructures, which can significantly enhance the local electromagnetic field and therefore amplify the Raman signals of analysts by several orders of magnitude. The classic SERS substrates are coinage-metals (Ag, Au, et al.) with uniform distribution nanostructures due to the excitation of localized surface plasmon resonances (LSPRs) on the surface of these metals [4–10]. However, the nanofabrication methods for producing the elaborate nanostructures of the SERS materials such as nanoparticles or arrays often involve multiple complex steps with the high cost and pollution, largely limiting the enormous application of SERS technique. In recent years, many novel materials such as, the alkali metals, graphene, semiconductors and quantum dots used as SERS substrates were explored [11–15]. These materials are either highly reactive in air (alkali metal) or have low enhanced effects (graphene, semiconductors and quantum dots) due to the pure chemical enhancements instead of electromagnetic enhancements (EM) caused by LSPRs. Developing the low-cost SERS substrate with excellent surface enhanced effect and the simple preparation process, still presents a major challenge.

As a new class of amorphous materials, metallic glasses (MGs) have absorbed considerable attentions due to their attractive properties such as high strength, large elastic limit, excellent corrosion and wear resistance. With the lack of crystalline defects in the disordered atomic structure and almost zero volume shrinkage during glass transition, MGs can be processed and shaped in the supercooled liquid region with a high precision down to the atomic scale. Therefore, MGs are regarded as an ideal material for the fabrication of elaborate nanostructures and nano-devices [16, 17]. Moreover, arising from the non-equilibrium nature, the atoms on the surface of MGs are often in a high-energy and activate state, which results in some unique properties that are highly desirable in many chemical processes. For example, recent studies showed that MGs can be used as efficient electrocatalyst for the degradation of water contaminants as well as electrochemical splitting of water [18–20].

Here, we reported a stable and low-cost butterfly-wing hierarchical MG nanostructure by vapor deposition technique. The MG nanostructure could show an enhanced surface Raman scattering effect and moreover, an excellent superhydrophobicity and self-cleaning behavior. These combined properties render MGs as a new efficient SERS material with low cost and good durability. The underlying mechanism for the SERS effect of MG nanostructure was also discussed in terms of their intrinsic chemical inhomogeneity and active atomic sites. The finite-difference time-domain (FDTD) simulation affirms that the enhancement of localized electromagnetic field at the gap between the adjacent MG nanoparticles (NPs).

Address correspondence to Lin Gu, l.gu@iphy.ac.cn; Baoan Sun, sunba@iphy.ac.cn

2 Experimental section

2.1 Materials

The Zr-based deposition target with a size of 100 mm × 100 mm × 2 mm was fabricated by copper-mold-casting method in an argon atmosphere. The purity of Ag material bought from a commercial company is 99.99%. The wing scales from *Papillo Paris* (*P. Paris*) is chosen as original bio-templates to replicate. To remove the possibly existing oxide layer on the target surface, pre-sputtering was carried out for 300 s, then MG film was deposited on wing scales. The ion beam current and energy was 20 mA and 750 eV, respectively. The deposition rate is about 4.5 nm/min. The pressure of chamber is lower than 2×10^{-4} Pa, and the depositing argon pressure is 2.4×10^{-2} Pa.

2.2 Characterization

The vitrification nature of the samples was ascertained by X-ray radiation (MAC Mo_3 XHF diffractometer with Cu Kα-radiation). EDS analysis and SEM images were carried out using a Phenom XL (15 kV). TEM images were conducted on a JEOL 2100 Plus (200 kV). The water contact angle was measured by a Dataphysics OCA20 contact angle system. The water droplet of 1 μL is dropped on the surface of MG replicas. Images are captured by digital cameras and then the static water contact angles are calculated by tangent method. UV–vis absorbance spectra were recorded with a HITACHI UV-3900H spectrometer. The bare butterfly wing is used as a reference during the measurement of UV–vis absorbance spectra.

2.3 Measurement of Raman scattering spectra

Rhodamine 6G (R6G) powders were dissolved into deionized water to form solutions with different concentrations. The MG or pure Ag replicas were immersed in R6G solutions for 1 h, upon which the samples were taken out and then dried. The Raman spectra were recorded using a micro-Raman spectrometer (Horiba/Jobin Yvon HR 800) equipped with 532 nm laser as the excitation source (laser power: 1 mW and laser spot size: 2 μm). The data acquisition time was 10 s.

3 Results and discussion

Figures 1(a)–1(c) give an illustration for the fabrication of the MG nanostructure. The fabrication procedure is pretty simple, only involving one step of depositing the MG target materials onto a butterfly wing specimen. Here, we chose the *P. Paris* butterfly specimen whose dorsal surface displays a prominent shining metallic green area with fine nanostructures. The alloy compositions for the target materials are $(Zr_{46}Cu_{46}Al_8)_{100-x}Ag_x$ ($5 < x < 64$, in atomic percent). The $Zr_{46}Cu_{46}Al_8$ alloy has been reported to have an excellent glass-forming ability, while the reason for doping Ag into the alloy is to utilize the intrinsic LSPR of Ag, and for the sake of the comparison with the pure crystal Ag. The alloy targets with designed shape were first prepared by a high-vacuum arc-melting system and then suck casting into a copper mold. Then metallic films were obtained by depositing the target materials into the dorsal surface of butterfly wings with an ion beam assisted deposition (IBAD) technique (for details see Experimental section). Figure 1(d) shows that the performance measurements directly were conducted on the surface of deposited film.

Figures 1(e) and 1(f) are typical micrographs of the deposited film obtained by scanning electron microscopy (SEM). As can be seen, the complex hierarchical structure of dorsal forewing is fully replicated by the deposited metallic film. At low magnification, the film structure is composed of many regular scaly structures with a typical size of 100 μm (Fig. 1(e)). While examined under a high magnification, each scaly in fact contains many fine nanostructures including main ridges, ribs and irregular holes (Fig. 1(f)). The ribs have an average thickness of 250 nm, while the hole size ranges from 200 nm to 2 μm. Figure 1(g) also gives a 3-dimensional profile for the nanostructures probed by SEM. The average roughness for the nanostructures is about 400 nm obtained from the height plot along the diagonal as shown in Fig. 1(h). These results confirm the formation of complex hierarchical metallic nanostructures on the biological template by the IBAD technique. In addition, the IBAD technique could produce the film with a composition close to that of the target material, which is particularly for multicomponent alloy systems. As shown by the energy dispersive X-ray spectrometry (EDS) (see Fig. S1 the in Electronic Supplementary Material (ESM)), the average composition for the deposited film is measured to be $(Zr_{46}Cu_{46}Al_8)_{82}Ag_{18}$, which is very close to the original composition of the target alloy $(Zr_{46}Cu_{46}Al_8)_{80}Ag_{20}$. Moreover, EDS mapping shows that each element is homogeneously distributed across the analyzed area without composition segregation. Compared with other methods for producing analogous periodic metallic nanostructures, e.g., electroless plating or electroplating, IBAD method is an effective approach to replicate the bio-template with multicomponent alloy [7, 21–30].

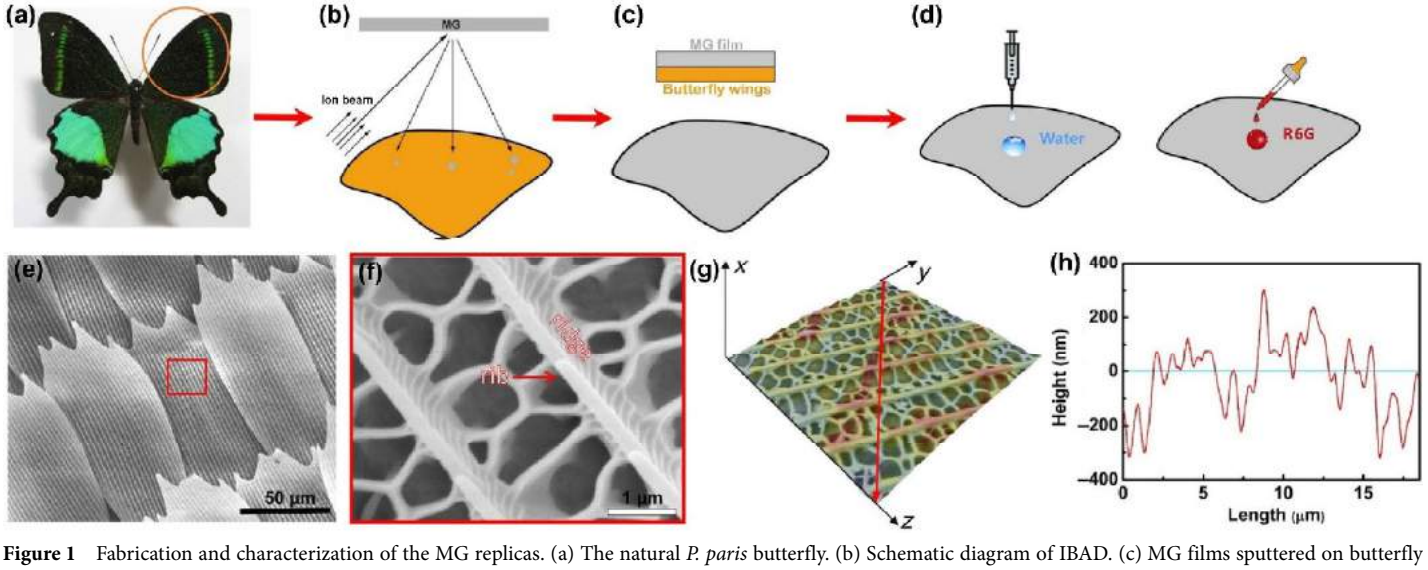

Figure 1 Fabrication and characterization of the MG replicas. (a) The natural *P. paris* butterfly. (b) Schematic diagram of IBAD. (c) MG films sputtered on butterfly forewings. (d) The experiments of superhydrophobicity and SERS. (e) SEM image of the $(Zr_{46}Cu_{46}Al_8)_{82}Ag_{18}$ MG scale replicas. (f) Hierarchical patterns of scale in red box of (e). (g) 3-Dimensional view of SEM image of (f). (h) The roughness along the red arrow in (g).

The amorphous nature of the metallic films was characterized by X-ray diffraction (XRD) and transmission electron microscopy (TEM), as shown in Fig. 2. From the XRD profiles, one can see that when the content of Ag is below 36 at.%, the metallic replicas display a full amorphous structure, manifested as a broad amorphous peak in the XRD curves (Fig. 2(a)). While at 50 at.% Ag content, the deposited replica displays obvious crystalline peaks in the broad amorphous peak. This suggests that the glass-forming ability of the deposited metallic replicas is generally decreased with the increasing Ag content. The results are further confirmed by TEM. The samples for TEM are directly taken out from the scales of alloy replicas and thinned by focus ion beam (FIB) (Fig. S2 in the ESM). As can be seen from Figs. 2(b) and 2(c), $(Zr_{46}Cu_{46}Al_8)_{64}Ag_{36}$ replicas display a maze-like structure in the bright field image and dispersed diffraction halo in the corresponding SAED, which are typical features of an amorphous structure. While the replicas with 50 at.% of Ag shows the crystalline lattice and diffraction spots. According to the fast Fourier transform (FFT) of enlarged TEM image, the nanocrystals are identified as Ag_4Al (Fig. 2(d)). The nanocrystallization of $(Zr_{46}Cu_{46}Al_8)_{50}Ag_{50}$ replicas can be attributed to the low glass forming ability of the alloy and the suppressed cooling rate during deposition due to the non-conductivity of biological substrate.

The SERS performance of these metallic replicas was measured and analyzed. R6G was used as a model analyte to collect the SERS signals. The UV–vis spectroscopy was used to characterize the LSPR properties of MG replicas before Raman collections (Fig. S3 in the ESM). The spectrum of MG replicas with deposition time of 5 min shows a clear absorption peak around 300 nm and a broad LSPR absorption band around 500 nm. When the deposition time increases, the broad LSPR absorption band disappears in the optical absorption spectrum, which is attributed to the change of nanogap between main ridges or diameter of irregular holes. In general, the thin MG replicas shows the better LSPR properties than the thick one, which is consistent with the change of Raman intensity with the deposition time (Fig. S4 in the ESM). The peaks shown in Raman spectrum all coming from R6G molecule have been enhanced by the MG nanostructures. Therefore, the MG replicas with the deposition time of 5 min are chosen as SERS substrates. The detection limit is a significant important parameter for evaluating the overall performance of SERS substrates. To determine the detection limit of the MG replicas, four identical substrates were exposed to R6G solutions, respectively, with concentration varying from 10^{-4} to 10^{-10} M for 1 h (Fig. 3(a)). The intensity of two different Raman shifts at 610 and 1,650 cm^{-1} are used for the indexes to detect the SRES limit. As can be seen from Fig. 3(b), even for a concentration of R6G solution as low as 10^{-8} M, the typical Raman peaks of R6G solution can still be observed for $(Zr_{46}Cu_{46}Al_8)_{82}Ag_{18}$, suggesting a high detection sensitivity of the MG replicas. To further calculate the limit of detection (LOD), the calibration curve of average peak intensities at the 1,650 cm^{-1} against the logarithmic concentration of R6G for $(Zr_{46}Cu_{46}Al_8)_{82}Ag_{18}$ MG replicas is shown in Fig. S6 in the ESM. Based on the definition of LOD, the detection limit is calculated to be about 6.6×10^{-9} M (The calculation details see Text SI and Fig. S6 in the ESM) [31].

Figure 3(c) compares the SERS performance of the alloy replicas with different Ag contents with a solution concentration of 10^{-6} M. The variation of Raman intensity (at 610 and 1,650 cm^{-1}) with different Ag contents are shown in Fig. 3(d). One can see that the Raman intensity initially increases with the content of Ag, and reaches a maximum at 36 at.% of Ag content, then dramatically decreases. Coincidently, after 36 at.% of Ag content, the structure of replicas is also transformed from fully amorphous to a composite structure with the precipitation of nanocrystals. The SERS effect of amorphous replicas should be originated from the intrinsic LSPR property of Ag. This can be evidenced by that the SERS effect cannot be observed in the $Cu_{50}Zr_{50}$ MG replicas without Ag (Fig. S5 in the ESM). So, it is natural that the SERS effect of the replicas increases with the Ag content as the replicas structure is still fully amorphous. While the dramatically decreased SERS after 36 at.% of Ag content suggests that the amorphous state of replicas films can be largely contributed to the SERS. To confirm this, we also measured the SERS spectra of

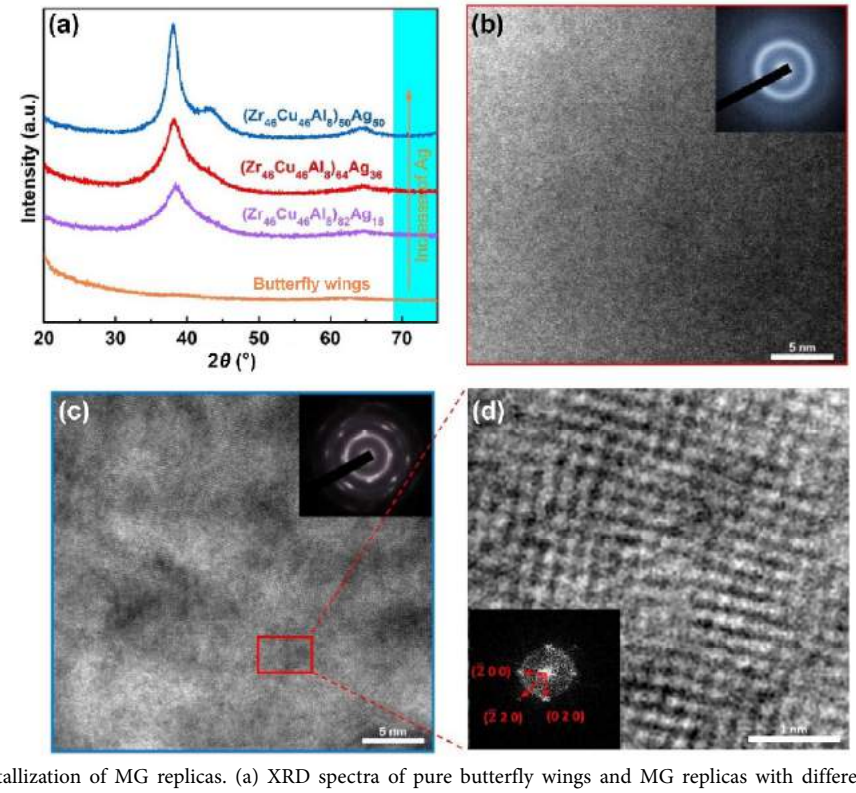

Figure 2 Examination of crystallization of MG replicas. (a) XRD spectra of pure butterfly wings and MG replicas with different Ag content. TEM images and corresponding SAED of alloy replicas of (b) $(Zr_{46}Cu_{46}Al_8)_{64}Ag_{36}$ and (c) $(Zr_{46}Cu_{46}Al_8)_{50}Ag_{50}$. (d) Enlarged TEM image of the red region marked in (c) with its FFT image inset.

other alloy replicas with different Ag contents (Fig. S5 in the ESM). One can see that the Raman intensity of the partially crystalized MG replicas, for both the Cu-based alloy with the same Ag content of 18 at.% and the Ag-based alloy with the high Ag content of 50 at.%, is far below that of the $(Zr_{46}Cu_{46}Al_8)_{82}Ag_{18}$ MG replicas.

To further illustrate the role of amorphous structure for the significant SERS properties of MG replicas, we compared the Raman performances of pure Ag and $(Zr_{46}Cu_{46}Al_8)_{82}Ag_{18}$ MG replicas with similar hierarchical nanostructures both fabricated by the IBAD. The measured Raman signals of 10^{-4} M R6G absorbed on the two samples are shown in Fig. 4(a) and the Raman intensity at 610 and 1,650 cm^{-1} for the pure Ag and $(Zr_{46}Cu_{46}Al_8)_{82}Ag_{18}$ MG replicas are given in Fig. 4(b). It should be noted that even with a low Ag content, the Raman intensity of $(Zr_{46}Cu_{46}Al_8)_{82}Ag_{18}$ MG replicas is the same order as that of the pure Ag one, indicating the significant contribution of the amorphous structure to SERS. To quantify this,

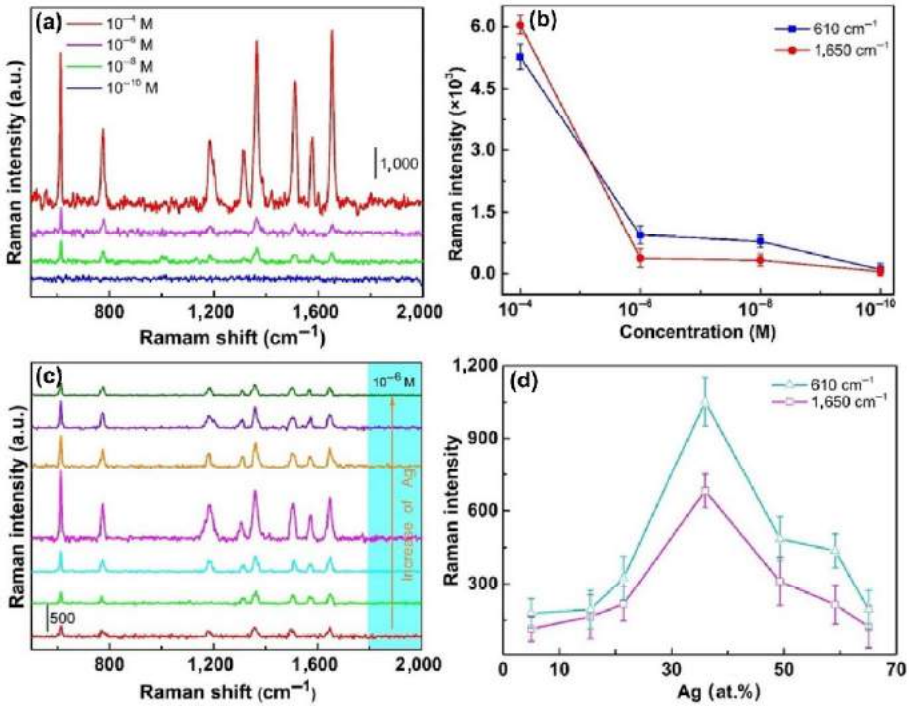

Figure 3 SERS measurements and intensity analysis of alloy replicas. (a) SERS spectra of 10^{-4}, 10^{-6}, 10^{-8} and 10^{-10} M R6G collected on the $(Zr_{46}Cu_{46}Al_8)_{82}Ag_{18}$ MG replicas. (b) Raman intensity of (a) at 610 and 1,650 cm^{-1} as a function of concentration (in logarithmic scale). (c) SERS spectra of 10^{-6} M R6G for alloy replicas with different Ag: $(Zr_{46}Cu_{46}Al_8)_{95}Ag_5$, $(Zr_{46}Cu_{46}Al8)_{84}Ag_{16}$, $(Zr_{46}Cu_{46}Al_8)_{78}Ag_{22}$, $(Zr_{46}Cu_{46}Al_8)_{64}Ag_{36}$, $(Zr_{46}Cu_{46}Al_8)_{50}Ag_{50}$, $(Zr_{46}Cu_{46}Al_8)_{40}Ag_{60}$, and $(Zr_{46}Cu_{46}Al_8)_{35}Ag_{64}$. (d) Raman intensity of (c) for different component.

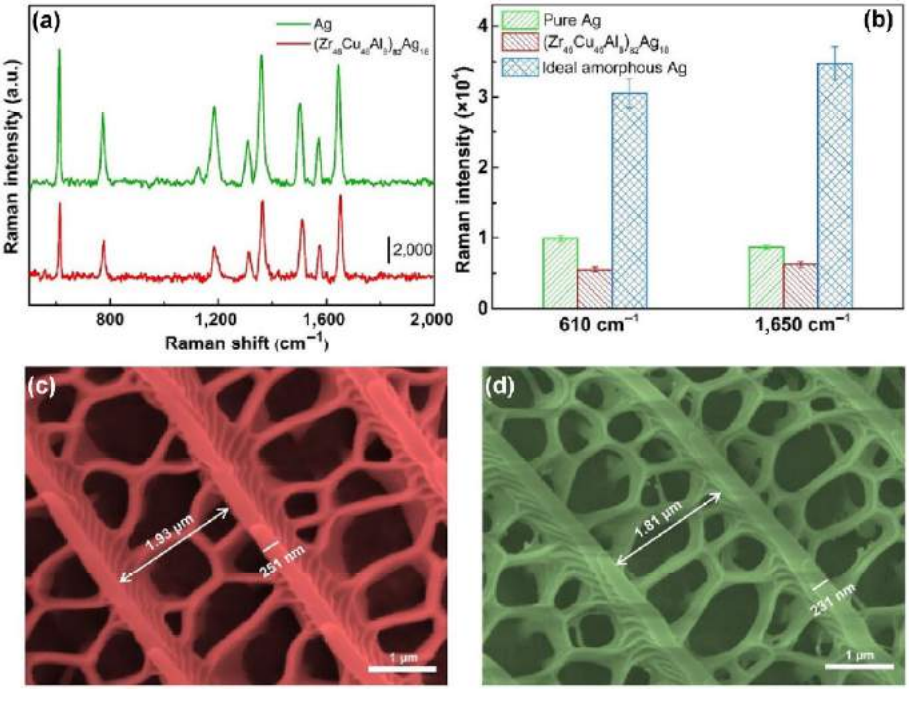

Figure 4 SERS measurements and morphology of the pure Ag and MG replicas. (a) Comparison of SERS signals from 10^{-4} M R6G on the pure Ag and $(Zr_{46}Cu_{46}Al_8)_{82}Ag_{18}$ MG replicas. (b) Raman intensity at peaks of the replicas of pure Ag (green bar), $(Zr_{46}Cu_{46}Al_8)_{82}Ag_{18}$ MG (red bar) and ideal amorphous Ag (blue bar). SEM images of (c) the MG replicas and (d) pure Ag replicas.

we estimated the Raman performance of the ideal amorphous Ag replicas by simply scaling the Raman intensity of $(Zr_{46}Cu_{46}Al_8)_{82}Ag_{18}$ MG replicas according to the Ag content, also shown in Fig. 4(b). Obviously, if the pure Ag is in an amorphous state, the SERS performance of the replicas will be much better than that of the pure Ag crystalline replicas. We also examine the microstructure of the pure Ag and MG replicas by SEM, as shown in Figs. 4(c) and 4(d), respectively. The width of ribs and the distance between them for the pure Ag replicas are similar with those of MG replicas. This excludes the possibility that the surface microstructures result in the enhancement of Raman signals for MG replicas. Therefore, the fundamental mechanism of the superior SERS for the MG replicas should be related to the amorphous nature.

For the practical application in SERS, the self-cleaning behavior of the MG replicas is also important, which could facilitate the concentration of analyst within the small contact area before SERS collection and easily washed away from the surface after the SERS collection [24, 26, 29]. Therefore, we also measured the surface wettability of MG replicas with excellent SERS performance as well as a smooth MG film deposited on silicon wafer for comparison. As shown in Fig. 5, the contact angle of the MG replica is about 140°, which is almost 40° larger than that of the flat MG film, indicating the superior self-cleaning behavior of the MG replicas when contacting with some liquids. The superhydrophobicity of MG inheriting from the nanostructures of butterfly wing offers great advantages for surface self-clean and extends the SERS service life in practical applications [32–35].

To understand the pronounced SERS effects induced by the amorphous structure, the physical mechanism for the SERS effect of nanostructured coinage-metals should be firstly discussed. In principle, the SERS arises from the localized electromagnetic enhancement for the incident light at some hotspots [4, 36, 37]. Due to the intrinsic LSPR properties of noble metals, a single or coupled of their nanostructures with small sizes (1–5 nm) could act as the hotspots for the enhancement of local electromagnetic field, leading to the enhanced Raman scattering from the molecular in the nanogap [5, 38–41]. Arising from the metastable nature, the structure of MGs is intrinsically inhomogeneous at the nanoscale. This has been recently verified by many studies with time-resolved techniques [42–44]. There are closely packed atomic clusters (e.g., icosahedrons) (hard regions) and loosely packed sites (soft regions) between them in the structural heterogeneity. Due to the loosely packed structure and the relatively high energy state, it is possible that the small chemical molecules are attached at these soft nanoscale regions (Fig. 6).

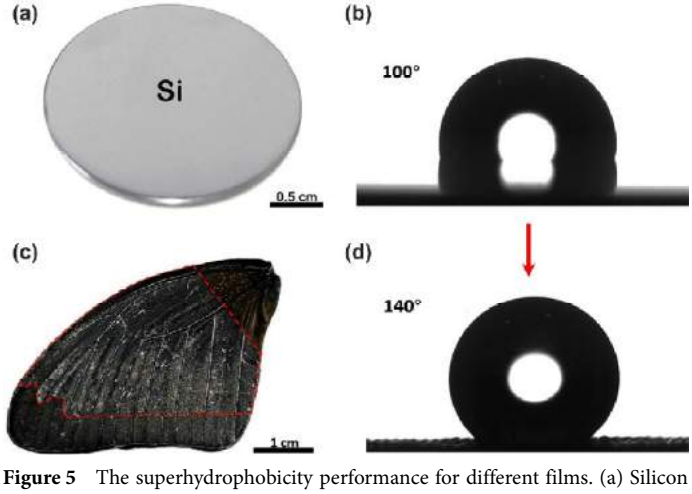

Figure 5 The superhydrophobicity performance for different films. (a) Silicon wafer with the $(Zr_{46}Cu_{46}Al_8)_{82}Ag_{18}$ MG film. (b) The contact angle of MG film deposited on silicon wafer is about 100°. (c) The $(Zr_{46}Cu_{46}Al_8)_{82}Ag_{18}$ MG replicas circled by the red region. (d) The MG replicas in (c) show superhydrophobicity with the contact angle of 140°. The measurement error is less than 5°.

While the "hotspots" are generated by the gap-dependent EM field coupling among the adjacent closely packed atomic clusters (1–2 nm in size), as shown in Fig. 6(a), similar to nanoparticles of noble metals. By this way, the Raman-scattered light of R6G molecules between these nanoclusters consist of a few atoms is amplified by the local strong electromagnetic field.

The 3D finite-difference time-domain (FDTD) simulation was introduced to prove the electric field enhancement between MG nano-clusters. The insertion diagram in Fig. 6(b) shows the structural model for the FDTD simulation. The dielectric coefficient of MG nano-clusters is fitted from the measurement data which is shown in Fig. S7 in the ESM. Here, we treated the densely-packed atomic clusters in the amorphous structure of MGs as NPs with a size of 2 nm. Then we calculate the variation of the maximum and average electric field enhancement factor $|E/E_0|^4$ with the gap distance of MG NPs. The more details of simulation can be found in text SII in the ESM. In the simulation, the incident plane wave with a wavelength range from 250 to 700 nm propagates along the z axis direction and its polarization direction is parallel to the x axis (Fig. 6(b)). To make sure that the gap was meshed correctly, a mesh override with very fine step was used. Figure 6(b) shows the variation for the maximum and average electric field enhancement factors ($|E/E_0|^4$) with the change of gap distance between two adjacent MG NPs, where $|E/E_0|^4$ increases nonlinearly with the decrease of the gap. When the gap is less than 2 nm, the maximum $|E/E_0|^4$ values decline sharply with the increase of the gap, then towards stability for the gap greater than 2 nm. So does the mean $|E/E_0|^4$ values, while the gap of 2 nm just corresponds to the size of soft or liquid-like regions in the amorphous structure of MGs as reported by previous literatures [45–48]. All these evidences indicate that the MG NPs will significantly improve the electric field enhancement (increased by more than 20 times). Moreover, the electrical field intensity distributions of MG NPs with 0.6 and 4 nm gap in the vertical plane (x–z) are shown in Figs. 6(c) and 6(d), respectively. It can be clearly seen that the localized electric field is mainly confined into the nanogap between the adjacent MG NPs.

In general, the excellent SERS of the MG butterfly-wing nanostructures is a combination of three effects: the intrinsic LSPR of Ag atom, the atomic-scale structural inhomogeneities of MGs and the large surface area of the hierarchical butterfly-wing structure. Every factor plays a key role in the superior SERS effect. As shown in Fig. S8 and Text SIII in the ESM, the hierarchical structure of butterfly scales results in a specific surface area 20 times larger than that of the flat surface, which further greatly enhances the SERS effect caused by the adjacent MG NPs. If the original biostructures are destroyed, i.e., the surface becomes smooth, the measured SERS signal is very weak and almost can be neglected (Fig. S9 in the ESM).

4 Conclusion

In summary, we successfully fabricate a complex hierarchical MG nanostructure through replicating the structure of biomaterials. The MG nanostructure displays an excellent SERS effect, the superhydrophobicity and self-cleaning behavior. The SERS effect of the MG nanostructure is related to the intrinsic structural heterogeneities on the MG surface, which provides a large number of hotspots for the amplification of the localized electromagnetic field and Raman scattering enhancement. Our works show that the MG could be a new SERS material with low cost and good durability, which will well extend the functional application of this material.

Acknowledgements

The authors would like to thank the support of the National Natural Science Foundation of China (Nos. 51822107, 51671121, 51761135125, and 61888102), the National Key Research and

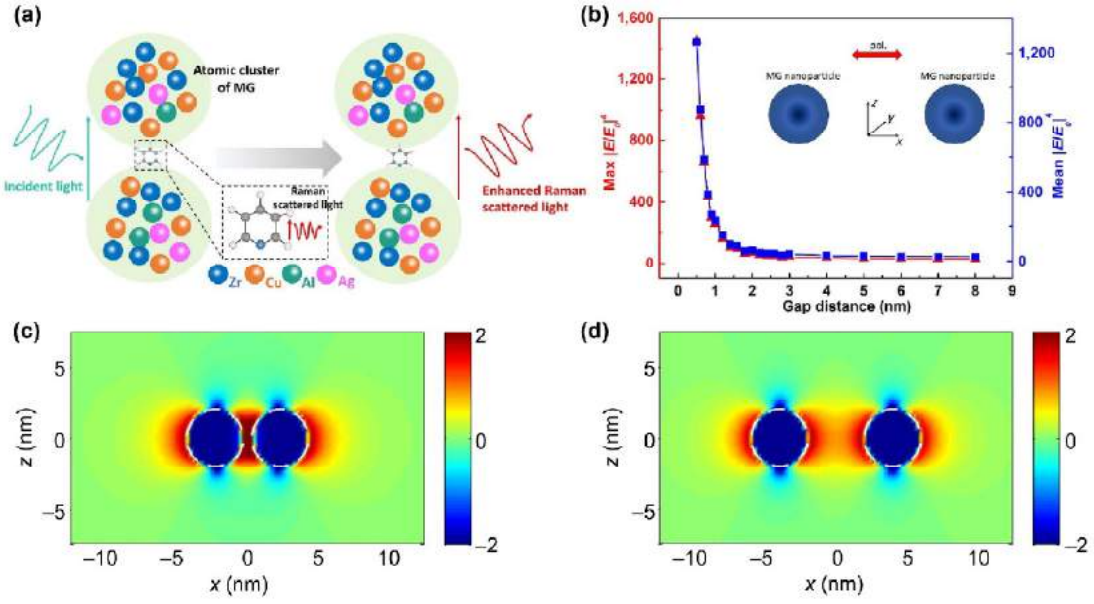

Figure 6 (a) Schematic illustration of the Raman experiments on R6G molecules on the $(Zr_{46}Cu_{46}Al_8)_{82}Ag_{18}$ MG replicas. The insertion diagram in (b) shows the structural model for the FDTD simulation. In the FDTD simulation, we set the diameter of the MG NPs as constant of 2 nm and the gaps of 0.5–8 nm. (b) The maximum and average electric field enhancement factor versus the gap distance of MG NPs. The electric field distribution (logarithmic scale) of the MG NPs with the gap of 0.6 (c) and 4 nm (d). The white dotted lines indicate the location of the MG NPs.

Development Program (No. 2018YFA0703603) and the Strategic Priority Research Program of the Chinese Academy of Sciences (Nos. XDB07030200 and XDB30000000). We appreciate Professor Di Zhang's deep discussions on the usage of bio-templates. The authors also thank Ruhao Pan and Xianzhong Yang for discussions on collecting Raman spectra, Mo Han Wang for the measurement of UV–vis absorption spectra and Kun Chen for the dielectric coefficient measurement.

Electronic Supplementary Material: Supplementary material (Text SI: calculation of the limit of detection; Text SII: FDTD simulation details; Text SIII: estimation of specific surface area, and Figs. S1–S9) is available in the online version of this article at https://doi.org/10.1007/s12274-019-2517-2.

References

[1] Goldberg-Oppenheimer, P.; Mahajan, S.; Steiner, U. Hierarchical electrohydrodynamic structures for surface-enhanced Raman scattering. *Adv. Mater.* **2012**, *24*, OP175–OP180.

[2] Sharma, B.; Frontiera, R. R.; Henry, A. I.; Ringe, E.; Van Duyne, R. P. SERS: Materials, applications, and the future. *Mater. Today* **2012**, *15*, 16–25.

[3] Stiles, P. L.; Dieringer, J. A.; Shah, N. C.; Van Duyne, R. P. Surface-enhanced Raman spectroscopy. *Annu. Rev. Anal. Chem.* **2008**, *1*, 601–626.

[4] Ding, S. Y.; Yi, J.; Li, J. F.; Ren, B.; Wu, D. Y.; Panneerselvam, R.; Tian, Z. Q. Nanostructure-based plasmon-enhanced Raman spectroscopy for surface analysis of materials. *Nat. Rev. Mater.* **2016**, *1*, 16021.

[5] Li, J. F.; Huang, Y. F.; Ding, Y.; Yang, Z. L.; Li, S. B.; Zhou, X. S.; Fan, F. R.; Zhang, W.; Zhou, Z. Y.; Wu, D. Y. et al. Shell-isolated nanoparticle-enhanced Raman spectroscopy. *Nature* **2010**, *464*, 392–395.

[6] Li, J. F.; Zhang, Y. J.; Rudnev, A. V.; Anema, J. R.; Li, S. B.; Hong, W. J.; Rajapandiyan, P.; Lipkowski, J.; Wandlowski, T.; Tian, Z. Q. Electrochemical shell-isolated nanoparticle-enhanced Raman spectroscopy: Correlating structural information and adsorption processes of pyridine at the Au(hkl) single crystal/solution interface. *J. Am. Chem. Soc.* **2015**, *137*, 2400–2408.

[7] Mo, X.; Wu, Y. W.; Zhang, J. H.; Hang, T.; Li, M. Bioinspired multifunctional Au nanostructures with switchable adhesion. *Langmuir* **2015**, *31*, 10850–10858.

[8] Oh, Y. J.; Jeong, K. H. Glass nanopillar arrays with nanogap-rich silver nanoislands for highly intense surface enhanced Raman scattering. *Adv. Mater.* **2012**, *24*, 2234–2237.

[9] Wang, H. H.; Liu, C. Y.; Wu, S. B.; Liu, N. W.; Peng, C. Y.; Chan, T. H.; Hsu, C. F.; Wang, J. K.; Wang, Y. L. Highly Raman-enhancing substrates based on silver nanoparticle arrays with tunable sub-10 nm gaps. *Adv. Mater.* **2006**, *18*, 491–495.

[10] Yang, X. Z.; Yu, H.; Guo, X.; Ding, Q. Q.; Pullerits, T.; Wang, R. M.; Zhang, G. Y.; Liang, W. J.; Sun, M. T. Plasmon-exciton coupling of monolayer MoS_2-Ag nanoparticles hybrids for surface catalytic reaction. *Mater. Today Energy* **2017**, *5*, 72–78.

[11] Kneipp, K.; Moskovits, M.; Kneipp, H. *Surface-Enhanced Raman Scattering: Physics and Applications*; Springer: Heidelberg, 2006.

[12] Li, J. F.; Anema, J. R.; Wandlowski, T.; Tian, Z. Q. Dielectric shell isolated and graphene shell isolated nanoparticle enhanced Raman spectroscopies and their applications. *Chem. Soc. Rev.* **2015**, *44*, 8399–8409.

[13] Ling, X.; Xie, L. M.; Fang, Y.; Xu, H.; Zhang, H. L.; Kong, J.; Dresselhaus, M. S.; Zhang, J.; Liu, Z. F. Can graphene be used as a substrate for Raman enhancement? *Nano Lett.* **2010**, *10*, 553–561.

[14] Shan, Y. F.; Zheng, Z. H.; Liu, J. J.; Yang, Y.; Li, Z. Y.; Huang, Z. R.; Jiang, D. L. Niobium pentoxide: A promising surface-enhanced Raman scattering active semiconductor substrate. *NPJ Comput. Mater.* **2017**, *3*, 11.

[15] Zhang, X.; Shi, C. S.; Liu, E. Z.; Li, J. J.; Zhao, N. Q.; He, C. N. Nitrogen-doped graphene network supported copper nanoparticles encapsulated with graphene shells for surface-enhanced Raman scattering. *Nanoscale* **2015**, 7, 17079–17087.

[16] Kumar, G.; Desai, A.; Schroers, J. Bulk metallic glass: The smaller the better. *Adv. Mater.* **2011**, *23*, 461–476.

[17] Kumar, G.; Tang, H. X.; Schroers, J. Nanomoulding with amorphous metals. *Nature* **2009**, *457*, 868–873.

[18] Wang, J. Q.; Liu, Y. H.; Chen, M. W.; Xie, G. Q.; Louzguine-Luzgin, D. V.; Inoue, A.; Perepezko, J. H. Rapid degradation of Azo dye by Fe-based metallic glass powder. *Adv. Funct. Mater.* **2012**, *22*, 2567–1570.

[19] Liang, S. X.; Jia, Z.; Liu, Y. J.; Zhang, W. C.; Wang, W. M.; Lu J.; Zhang, L. C. Compelling rejuvenated catalytic performance in metallic glasses. *Adv. Mater.* **2018**, *30*, 1802764.

[20] Hu, Y. C.; Wang, Y. Z.; Su, R.; Cao, C. R.; Li, F.; Sun, C. W.; Yang, Y.; Guan, P. F.; Ding, D. W.; Wang, Z. L. et al. A highly efficient and self-stabilizing metallic-glass catalyst for electrochemical hydrogen generation. *Adv. Mater.* **2016**, *28*, 10293–10297.

[21] Tan, Y. W.; Gu, J. J.; Xu, L. H.; Zang, X. N.; Liu, D. X.; Zhang, W.; Liu, Q. L.; Zhu, S. M.; Su, H. L.; Feng, C. L. et al. High-density hotspots engineered by naturally piled-up subwavelength structures in three-dimensional copper butterfly wing scales for surface-enhanced Raman scattering detection. *Adv. Funct. Mater.* **2012**, *22*, 1578–1585.

[22] Xu, B. B.; Zhang, Y. L.; Zhang, W. Y.; Liu, X. Q.; Wang, J. N.; Zhang, X. L.; Zhang, D. D.; Jiang, H. B.; Zhang, R.; Sun, H. B. Silver-coated rose petal: Green, facile, low-cost and sustainable fabrication of a SERS substrate with unique superhydrophobicity and high efficiency. *Adv. Opt. Mater.* **2013**, *1*, 56–60.

[23] Qian, C.; Ni, C.; Yu, W. X.; Wu, W. G.; Mao, H. Y.; Wang, Y. F.; Xu, J. Highly-ordered, 3D petal-like array for surface-enhanced Raman scattering. *Small* **2011**, *7*, 1801–1806.

[24] Chou, S. Y.; Yu, C. C.; Yen, Y. T.; Lin, K. T.; Chen, H. L.; Su, W. F. Romantic story or Raman scattering? Rose petals as ecofriendly, low-cost substrates for ultrasensitive surface-enhanced Raman scattering. *Anal. Chem.* **2015**, *87*, 6017−6024.

[25] Mu, Z. D.; Zhao, X. W.; Xie, Z. Y.; Zhao, Y. J.; Zhong, Q. F.; Bo, L.; Gu, Z. Z. *In situ* synthesis of gold nanoparticles (AuNPs) in butterfly wings for surface enhanced Raman spectroscopy (SERS). *J. Mater. Chem. B* **2013**, *1*, 1607–1613.

[26] Huang, J. A.; Zhang, Y. L.; Zhao, Y. Q.; Zhang, X. L.; Sun, M. L.; Zhang, W. J. Superhydrophobic SERS chip based on a Ag coated natural taro-leaf. *Nanoscale* **2016**, *8*, 11487–11493.

[27] Tan, Y. W.; Gu, J. J.; Zang, X. N.; Xu, W.; Shi, K. C.; Xu, L. H.; Zhang, D. Versatile fabrication of intact three-dimensional metallic butterfly wing scales with hierarchical sub-micrometer structures. *Angew. Chem., Int. Ed.* **2011**, *50*, 8307–8311.

[28] Tanahashi, I.; Harada, Y. Silver nanoparticles deposited on TiO_2-coated cicada and butterfly wings as naturally inspired SERS substrates. *J. Mater. Chem. C* **2015**, *3*, 5721–5726.

[29] Zhang, Q. X.; Chen, Y. X.; Guo, Z.; Liu, H. L.; Wang, D. P.; Huang, X. J. Bioinspired multifunctional hetero-hierarchical micro/nanostructure tetragonal array with self-cleaning, anticorrosion, and concentrators for the SERS detection. *ACS Appl. Mater. Interfaces* **2013**, *5*, 10633−10642.

[30] Liu, X. J.; Zong, C. H.; Ai, K. L.; He, W. H.; Lu, L. H. Engineering natural materials as surface-enhanced Raman spectroscopy substrates for *in situ* molecular sensing. *ACS Appl. Mater. Interfaces* **2012**, *4*, 6599−6608.

[31] Zhu, C. H.; Meng, G. W.; Zheng, P.; Huang, Q.; Li, Z. B.; Hu, X. Y.; Wang, X. J.; Huang, Z. L.; Li, F. D.; Wu, N. Q. A hierarchically ordered array of silver-nanorod bundles for surface-enhanced Raman scattering detection of phenolic pollutants. *Adv. Mater.* **2016**, *28*, 4871–4876.

[32] Kong, T. T.; Luo, G. Y.; Zhao, Y. J.; Liu, Z. Bioinspired superwettability micro/nanoarchitectures: Fabrications and applications. *Adv. Funct. Mater.* **2019**, *29*, 1808012.

[33] Schmidt, M. S.; Hübner, J.; Boisen, A. Large area fabrication of leaning silicon nanopillars for surface enhanced Raman spectroscopy. *Adv. Mater.* **2012**, *24*, OP11–OP18.

[34] Yang, L. B.; Liu, H. L.; Ma, Y. M.; Liu, J. H. Solvent-induced hot spot switch on silver nanorod enhanced Raman spectroscopy. *Analyst* **2012**, *137*, 1547–1549.

[35] Wu, Y. W.; Hang, T.; Yu, Z. Y.; Gu, J. J.; Li, M. Quasi-periodical 3D hierarchical silver nanosheets with sub-10 nm nanogap applied as an effective and applicable SERS substrate. *Adv. Mater. Interfaces* **2015**, *2*, 1500359.

[36] Maier, S. A.; Brongersma, M. L.; Kik, P. G.; Meltzer, S.; Requicha, A. A. G.; Atwater, H. A. Plasmonics—A route to nanoscale optical devices. *Adv. Mater.* **2001**, *13*, 1501–1505.

[37] Willets, K. A.; Van Duyne, R. P. Localized surface plasmon resonance spectroscopy and sensing. *Annu. Rev. Phys. Chem.* **2007**, *58*, 267–297.

[38] Li, X. H.; Chen, G. Y.; Yang, L. B.; Jin, Z.; Liu, J. H. Multifunctional Au-coated TiO_2 nanotube arrays as recyclable SERS substrates for multifold organic pollutants detection. *Adv. Funct. Mater.* **2010**, *20*, 2815–2824.

[39] Xu, W. G.; Xiao, J. Q.; Chen, Y. F.; Chen, Y. B.; Ling, X.; Zhang, J. Graphene-veiled gold substrate for surface-enhanced Raman spectroscopy. *Adv. Mater.* **2013**, *25*, 928–933.

[40] Hanske, C.; Sanz-Ortiz, M. N.; Liz-Marzán, L. M. Silica-coated plasmonic metal nanoparticles in action. *Adv. Mater.* **2018**, *30*, 1707003.

[41] Yang, X. Z.; Li, J.; Zhao, Y. X.; Yang, J. H.; Zhou, L. Y.; Dai, Z. G.; Guo, X.; Mu, S. J.; Liu, Q. Z.; Jiang, C. M. et al. Self-assembly of Au@Ag core–shell nanocuboids into staircase superstructures by droplet evaporation. *Nanoscale* **2018**, *10*, 142–149.

[42] Wagner, H.; Bedorf, D.; Küchemann, S.; Schwabe, M.; Zhang, B.; Arnold, W.; Samwer, K. Local elastic properties of a metallic glass. *Nat. Mater.* **2011**, *10*, 439–442.

[43] Ye, J. C.; Lu, J.; Liu, C. T.; Wang, Q.; Yang, Y. Atomistic free-volume zones and inelastic deformation of metallic glasses. *Nat. Mater.* **2010**, *9*, 619–623.

[44] Liu, Y. H.; Wang, D.; Nakajima, K.; Zhang, W.; Hirata, A.; Nishi, T.; Inoue, A.; Chen, M. W. Characterization of nanoscale mechanical heterogeneity in a metallic glass by dynamic force microscopy. *Phys. Rev. Lett.* **2011**, *106*, 125504.

[45] Hwang, J. W.; Melgarejo, Z. H.; Kalay, Y. E.; Kalay, I.; Kramer, M. J.; Stone, D. S.; Voyles, P. M. Nanoscale structure and structural relaxation in $Zr_{50}Cu_{45}Al_5$ bulk metallic glass. *Phys. Rev. Lett.* **2012**, *108*, 195505.

[46] Miracle, D. B. A structural model for metallic glasses. *Nat. Mater.* **2004**, *3*, 697–702.

[47] Sheng, H. W.; Liu, H. Z.; Cheng, Y. Q.; Wen, J.; Lee, P. L.; Luo, W. K.; Shastri, S. D.; Ma, E. Polyamorphism in a metallic glass. *Nat. Mater.* **2007**, *6*, 192–197.

[48] Sheng, H. W.; Luo, W. K.; Alamgir, F. M.; Bai, J. M.; Ma, E. Atomic packing and short-to-medium-range order in metallic glasses. *Nature* **2006**, *439*, 419–425.